An experimental method to investigate coherent spiral vortices in the boundary layer over rotating bodies of revolution

Tambe, Sumit; Schrijer, Ferry; Rao, Arvind Gangoli; Veldhuis, Leo

DOI
10.1007/s00348-019-2756-8

Publication date
2019

Document Version
Final published version

Published in
Experiments in Fluids

Citation (APA)
Tambe, S., Schrijer, F., Rao, A. G., & Veldhuis, L. (2019). An experimental method to investigate coherent spiral vortices in the boundary layer over rotating bodies of revolution. *Experiments in Fluids*, *60*(7), Article 115. https://doi.org/10.1007/s00348-019-2756-8

Experiments in Fluids (2019) 60:115
https://doi.org/10.1007/s00348-019-2756-8

LETTER

An experimental method to investigate coherent spiral vortices in the boundary layer over rotating bodies of revolution

Sumit Tambe[1] · **Ferry Schrijer**[1] · **Arvind Gangoli Rao**[1] · **Leo Veldhuis**[1]

Received: 19 October 2018 / Revised: 13 May 2019 / Accepted: 4 June 2019

Abstract

Infrared thermography is applied to measure the spiral vortices in the boundary layer over a rotating cone under axial inflow. The data sets are analysed using proper orthogonal decomposition (POD). A criterion based on the signal-to-noise ratio is defined for the selection of relevant POD modes, such that a low-order reconstruction with reduced measurement noise is obtained without affecting the thermal footprint of the spiral vortices. The resulting reconstruction still includes the large-scale modulations in the local vortex strength, relating to low-frequency phenomena like amplification, changing vortex states, disturbances in outer flow, etc. The effect of coherent vortical structures is further separated from such phenomena by selective reconstruction of the POD modes based on the number of observed vortices (n) along the circumference. The counter-rotating nature of these vortices is confirmed by PIV measurements. The number of spiral vortices shows good agreement with previously reported methods in the literature. The spiral vortex angle is in good agreement with the previous methods at low rotation ratio (S), but deviates towards the direction of the local wall shear for high values of S.

Graphic abstract

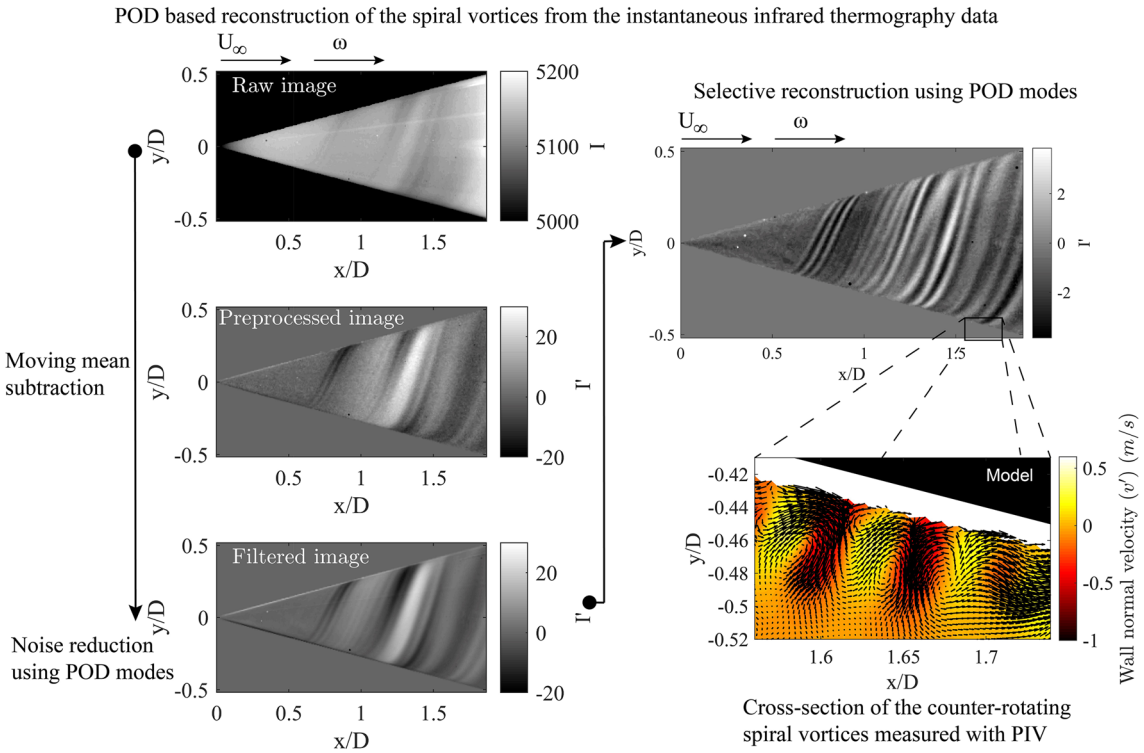

Extended author information available on the last page of the article

Published online: 18 June 2019

1 Introduction

When investigating coherent flow structures, flow visualization is an essential part to understand the underlying physical phenomena. Quantification of spatial properties such as: vortex angle, wavenumber, and the location of pairing or amplification is essential for the understanding and theoretical analysis. Experimental techniques which can provide such information have evolved over the years, but their applicability to rotating bodies is limited. For example, oil flow visualization, which is often used to identify flow features such as separation, reattachment, boundary layer transition, and the presence of stationary vortices, is not suitable for the rotating case due to the strong centrifugal forces. In the past, flow visualization was performed based on kerosene smoke filaments (Mueller et al. 1981) or titanium tetrachloride (Kobayashi et al. 1983) to identify spiral vortices in the transition region over rotating cones. However, smoke flow visualization works best only at low freestream velocities and low turbulence levels ($\sim 0.1\%$). On the other hand, titanium tetrachloride is very toxic and requires a highly controlled environment to avoid health issues. In addition, researchers have used hot-wire anemometry to quantify the spiral vortex characteristics and location of the transition region. However, such methods are intrusive in nature and time-consuming, which makes them less attractive for parametric studies. These experimental difficulties call for an alternative approach to enable in-depth study of the flow field over rotating bodies of revolution.

The motivation for the present study comes from the ongoing efforts to understand the interaction of distorted inflow with spinners and propulsors for novel aircraft configurations exploiting boundary layer ingestion, over the wing propulsors, etc. Here, the effect of inflow non-uniformity on the boundary layer of the spinners is not yet known. It is of interest to have an experimental method to quickly assess the boundary layer state for a given inflow condition. Therefore, in the present study, an experimental method is developed that can be used to detect flow features which can be linked to the presence of boundary layer instability on rotating bodies of revolution.

A rotating slender cone (half cone angle $\psi = 15°$) under uniform axial inflow is chosen as a test case, since it is well documented in the literature (Kobayashi et al. 1983; Kohama 1984). It is known that the boundary layer transition mechanism over the rotating cone includes spiral vortices that are induced by the effect of a centrifugal instability. The characteristics of these spiral vortices (angle and pitch) depend on the local velocity ratio, $S = \omega r / U_e$ and $Re_l = l U_e / \nu$, where ω is the angular velocity, r is the local radius, U_e is the edge velocity of the boundary layer, l is the distance from the cone apex along the meridian, and ν is kinematic viscosity of air. A brief overview of the flow field is given in Sect. 3. A further in-depth discussion about this flow field can be found in the literature (Kobayashi et al. 1983; Kohama 1984).

Infrared Thermography (IRT) is a non-intrusive technique which can be used to measure surface temperature distribution. The overall complexity of the setup and data post-processing is relatively low, which makes it attractive for the parametric studies that span a large number of experimental conditions. IRT has been previously applied to study stationary co-rotating spiral vortices on a rotating disk (Astarita et al. 2002). Limited by the recording frequency due to the scanning mechanism of the camera, the authors used a line scan method to acquire and later reconstruct the time-averaged imprint of spiral vortices. This approach was feasible, because the vortices were stationary with respect to the rotating disk. Nowadays, IR cameras use Focal Plane Arrays (FPA) which can record at higher frequencies and more importantly, no longer, require the scanning system. This allows using IR cameras for measuring high-speed events where the temporal averaging is only limited by the selected integration time. For example, in the current application, the vortices are not stationary but move along with the flow. Since the signal-to-noise ratio drops with decreasing integration time and high-speed events typically are less strong, the resulting measurements contain higher random noise. Recent investigations show that the potential of IRT can be dramatically enhanced by filtering the measurement data sets using proper orthogonal decomposition (POD). For example, Narayanan (2007) applied this methodology to study the modes of temperature fluctuations of slot jet impingement by filtering IRT data with first 15 POD modes. Ranc et al. (2015) demonstrated improvements in the signal-to-noise ratio of IRT measurements of a thermomechanical phenomenon by selecting physically admissible thermal modes from POD. Raiola et al. (2017) further developed the POD filter for time-resolved IRT measurements of turbulent convective heat transfer. They also proposed a criterion for selecting the optimal number of modes for the low-order reconstruction with reduced random noise. In the present study, IRT is applied to measure the traces of spiral vortices on a rotating cone and POD analysis is used to reduce noise and selectively reconstruct the flow features.

2 Experimental setup

Experiments are performed in the W-tunnel at the Faculty of Aerospace Engineering, TU Delft which is an open jet wind tunnel with an exit cross section of 600 mm × 600 mm. The model consists of a cone with an half cone angle $\psi = 15°$ and base diameter $D = 47$ mm. It was connected to a motor in a cylindrical casing mounted

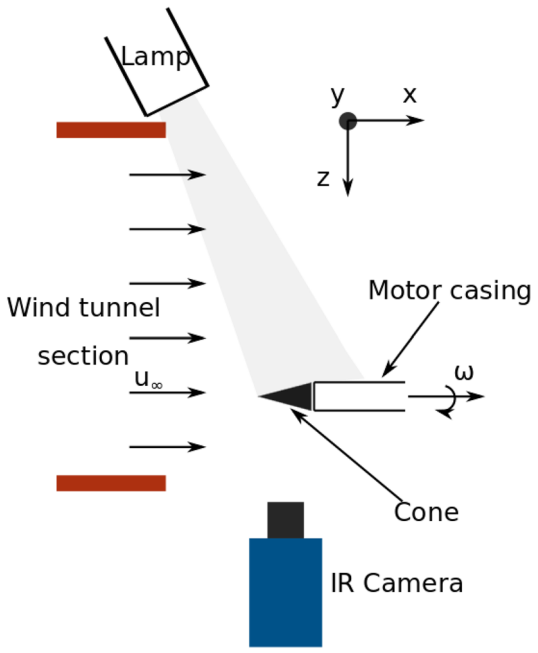

Fig. 1 Schematic of the experimental setup (top view)

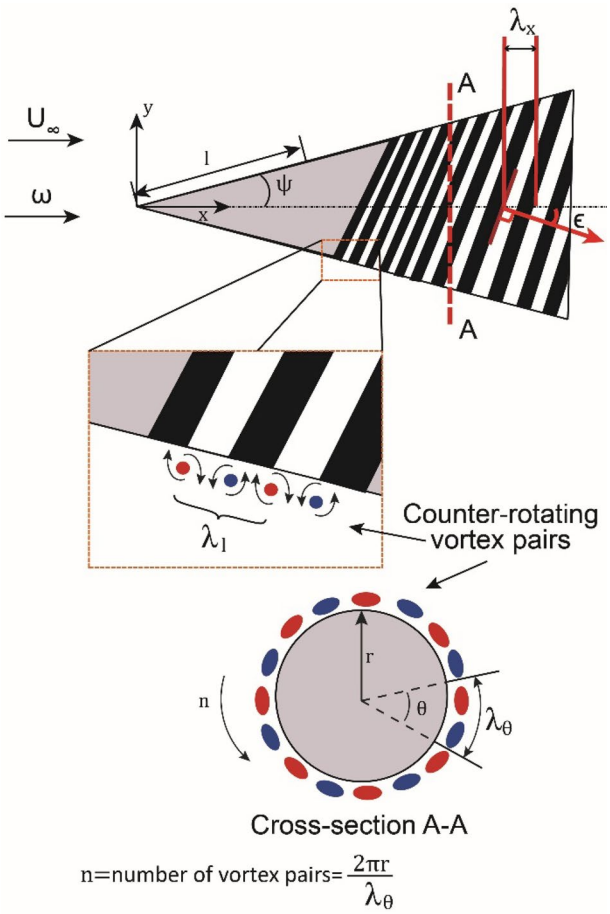

Fig. 2 Schematic representation of the flow field depicting typical footprints of the spiral vortices on the surface temperature along with the definitions of wavelength components (λ_l, λ_x, λ_θ), number of spiral vortices (n), and spiral vortex angle (ε). Effects of the surface curvature on the fringes is not shown for simplicity

on a sting. The cone was rotated by a brushless motor at a constant $RPM = 5000$. The inflow speed, U_∞, was varied from $2.46 - 12.3$ m/s to obtain different values of the ratio $S_b = \omega R_b / U_\infty$ (5–1, respectively), where R_b is the base radius. The diameter-based Reynolds number is defined as $Re_D = U_\infty D/\nu$. Additional tests are also performed at 15,000 RPM to assess the effect of surface rotation during the integration time. The characteristics of the spiral vortices strongly depend on the local value of S which varies along the cone from zero at the nose to $\omega R_b / U_e$ at the base. In the experiments, the value of S_b is used to characterise the flow conditions.

An Infrared camera FLIR (CEDIP) SC7300 Titanium is used to measure the surface temperature. As the focus of the present study is on the spatial organization of the coherent vortices, the temperature data are processed in the units of digital pixel intensity (I). The camera has a 320×256 pixel MCT sensor having a nominal Noise Equivalent Temperature Difference (NETD) < 25 mK. The spatial resolution for the measurements is 0.28 mm/px. An integration time of 205 µs is used and 2000 images are acquired at 200 Hz. The model was radiatively heated using a white light from a 575 W theatre lamp, which is focused on the model. Considering that the emissivity of the surface is highest in the direction normal to it, the camera (sensor plane) could be placed parallel to the side of the cone. However, this results in a strong reflection of the camera from the model surface (Narcissus effect) and, thus, reduces the quality of results. The camera placement was adjusted, so that the reflections from the model were minimized and the background noise from the light/heat source could be avoided. A schematic of the test setup is shown in Fig. 1. Once the lamp is switched on, the surface of the rotating model facing the lamp is irradiated and gets heated up. The surface that is not irradiated by the lamp is observed by the IR camera. The wind tunnel models are made from polyoxymethylene which has favourable thermal properties (thermal conductivity $\kappa = 0.22$ W/mK, density $\rho = 1420$ kg/m^3, and specific heat capacity $c = 1500$ J/kgK). Effect of directional emissivity on the observed digital intensity has been estimated by tracking intensity along the cone radius in the average image taken over a data set. Since, the cone surface is 3D, the viewing angle varies (with respect to the surface normal vector) from 15° at the axis and 90° at the outermost radial location. It has been observed that, within $R = 0 - 0.9R$, the intensity gradually drops by 10% (background is subtracted). However, from $0.9R - R$, it steeply drops to the

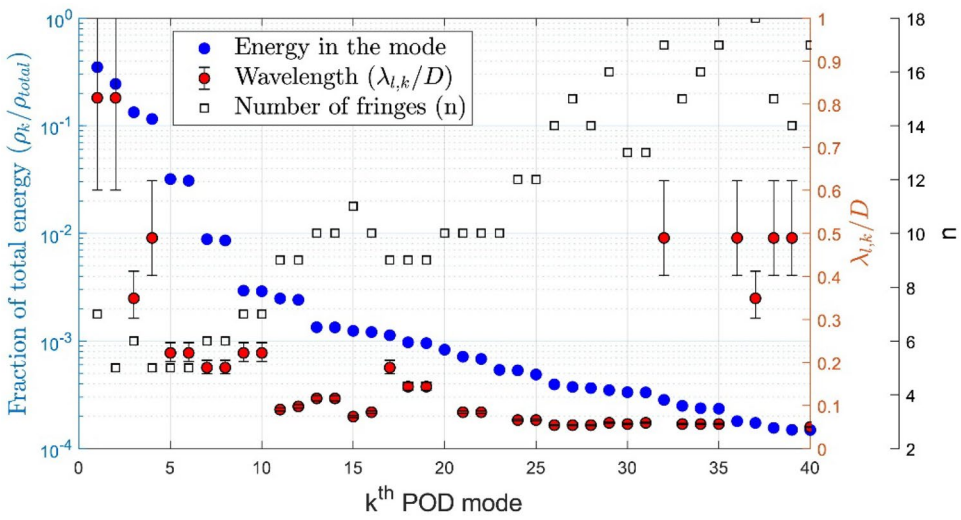

Fig. 3 Distribution of energy captured in each POD mode compared with the corresponding wavelength $(\lambda_{l,k})$ and the observed number of fringes $(n)\,(S_b = 5, Re_D = 7.4 \times 10^3, S = 0{-}4.71, Re_l = 0{-}1.58 \times 10^4)$

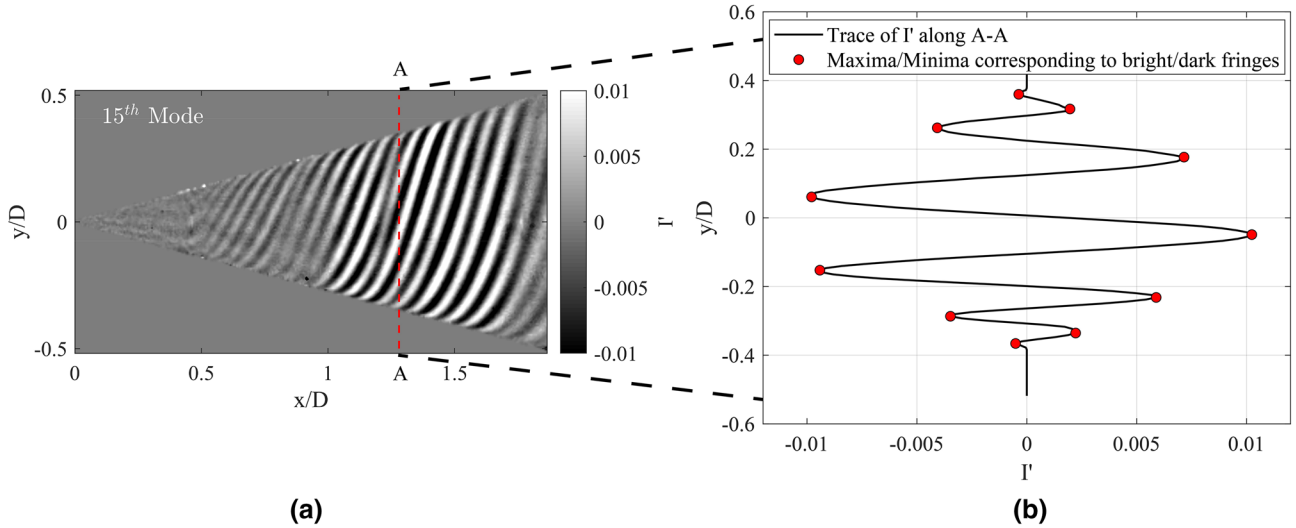

Fig. 4 Characteristics of a POD mode: **a** surface temperature field and **b** trace of I' along the circumference used to measure the number of fringes $(\boldsymbol{n})\,(S_b = 5, Re_D = 7.4 \times 10^3, S = 0{-}4.71, Re_l = 0{-}1.58 \times 10^4)$

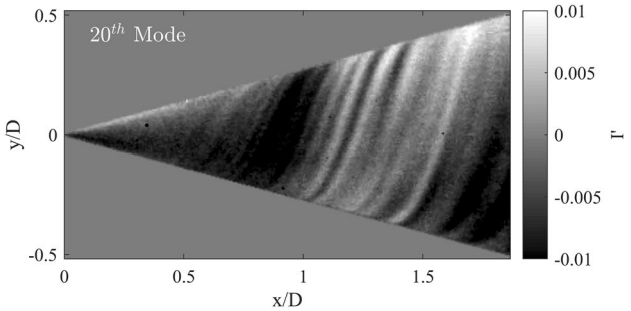

Fig. 5 The 20th POD mode $(S_b = 5, Re_D = 7.4 \times 10^3, S = 0{-}4.71, Re_l = 0{-}1.58 \times 10^4)$

background intensity. This region corresponds to the viewing angles beyond 65.23°. However, the main interest in the present investigation is the fluctuations over the time average for each pixel instead of the absolute magnitude.

It was observed that the overall surface temperature levels are not constant during the measurements, because the flow continuously cools down the model. Over the data set, this difference has been in the order of 5% of the mean intensity levels above the background. This trend is monotonic and has been removed by subtracting a moving average with a kernel size of 20 instances. The resulting temperature fluctuations over the cone surface correspond to the effect of

vortices and their magnitude is lower than 1.3 K. Furthermore, the IRT measurement data are analysed using proper orthogonal decomposition (POD), which decomposes the data set as a linear combination of spatial modes with time dependent coefficients. A detailed mathematical formulation of POD and different methods of obtaining basis functions (modes) can be found in the literature (Berkooz et al. 1993; Arányi et al. 2013).

In addition, time-resolved stereo particle image velocimetry (PIV) was used in the symmetry plane using two high-speed cameras (Photron Fastcam SA-1) to verify the results from IRT. The cameras have a 12 bit CMOS sensor with 1024×1024 pixels. SAFEX smoke particles with diameter ~ 1 µm are used as tracer particles. A Nd:YAG Continuum MESA PIV 532-120-M high-speed double pulsed laser is used to illuminate particles. The data are acquired at 2.5 kHz. The cameras were equipped with Nikkor$f = 200$ mm and Teleplus $2\times$ lenses resulting in an equivalent focal length of 400 mm. The field of view is 14 mm $\times$ 14 mm and the spatial resolution is 0.0136 mm/px. The data are processed using Lavision DAVIS 8.40 with a 48×48 pixels' final window size and 75% overlap, resulting in a vector pitch of 0.16 mm. The edge velocity of the boundary layer is obtained from the potential solution found in the study by Garrett and Peake (2007) as $U_e(x) = Cx^m$. Here, C and m are obtained by fitting this relation to the PIV data, which results in $C = 1.84U_\infty$ and $m = 0.23$.

3 Spatial characteristics of the spiral vortices

Before discussing the data processing procedure, it is important to introduce the flow field at a conceptual level. From the previous studies of Kobayashi et al. (1983), it was found that the spiral vortices on a rotating cone appear in the form of counter-rotating vortex pairs. It has been observed in the present study that their footprint on the surface temperature appears in the form of alternating dark and bright fringes, corresponding to low and high relative temperatures, respectively (see Figs. 2, 8). These temperature variations are caused by the up- and down-wash created by the vortices which means that there is one vortex pair in between two consecutive bright (or dark) fringes. Figure 2 also shows the definitions of the spiral vortex characteristics such as the components of the wavelength $(\lambda_l, \lambda_\theta)$, the number of spiral vortices along the circumference (n), and spiral vortex angle (ε). The wavelength λ_l can be associated with a wave travelling along the cone meridian in the stream-wise direction. It is defined as the distance between two consecutive vortex pairs along the meridian, which is equal to the distance between their consecutive bright (or dark) surface footprints. The wavelength, λ_θ, is the wavelength along the azimuthal direction. However, in the experiments, we observe the two-dimensional projection of a three-dimensional cone surface. Therefore, the direct estimation of λ_l and λ_θ is not possible. The projection of λ_l on to the xy plane is measured from a two dimensional image as λ_x, where $\lambda_x = \lambda_l \cos(\psi)$. Whereas, λ_θ is represented in terms of the number of spiral vortices along the circumference: $n = 2\pi r/\lambda_\theta$, where, r is the local radius. The spiral vortex angle (ε) is defined as the angle between the vector perpendicular to the spiral vortex filament and the meridional plane.

4 Data processing procedure

While the raw IRT data show traces of the spiral vortices, it also contains footprints of the large-scale modulations of these vortices. Since the spiral vortices are convected over the cone due to the surrounding inflow, in some cases, their strength varies and results in an observed modulation of the local vortex strength. This also includes effects caused by changing vortex states or amplification. This makes it difficult to visualize the underlying structure of the spiral vortices. In addition, due to the lower integration time and low levels of temperature fluctuations, the measurements also contain noise. These problems are tackled by following a two-step procedure to reconstruct the individual snapshots by a limited selection of the POD modes. At a first step, spatial modes of POD up to a selected mode number are used to obtain a low-order reconstruction with reduced noise (see Sect. 4.2). In a second step, the POD modes representing the effects of the large-scale modulations are further excluded in the reconstruction to obtain the structure of the coherent spiral vortices (see Sect. 4.3). The selection criteria are detailed in Sects. 4.2 and 4.3. The spatial POD modes are obtained using a singular value decomposition applied to the empirical correlation matrix of the data set. The resulting spatial modes are ordered according to the energy content (ρ) (in terms of temperature fluctuations) where the strongest modes appear first. In addition, in the present case, it is also important to obtain the spatial characteristics (similar to λ_l, n) of each POD mode to comprehend the type of spatial periodicity that is captured in it. The detailed discussion on the characteristics of POD modes is presented in Sect. 4.1.

4.1 Spatial characteristics of the POD modes

The characteristics of a POD mode (e.g., captured energy, wavelength, and number of fringes along the circumference) are used to comprehend the type of phenomena that it represents. These characteristics are then used while

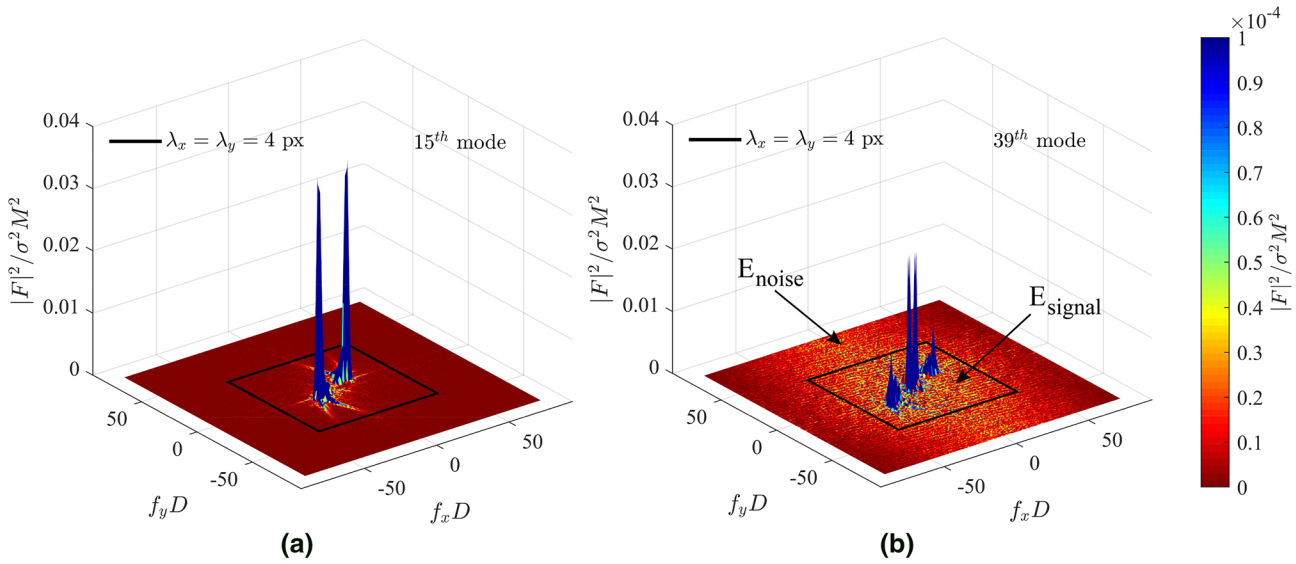

Fig. 6 Power spectral density (PSD) distribution obtained from 2D Fourier transform **a** 15th POD mode $E_{signal}/E_{noise} = 66.27$, $\rho_k/\rho_{Total} = 1.24 \times 10^{-3}$, $\phi_k = 0.082$, **b** 39th POD mode $E_{signal}/E_{noise} = 3.5$, $\rho_k/\rho_{Total} = 1.49 \times 10^{-4}$, $\phi_k = 0.00052$ $\left(S_b = 5, Re_D = 7.4 \times 10^3, S = 0\text{–}4.71, Re_l = 0\text{–}1.58 \times 10^4\right)$

defining selection criteria for the low-order reconstruction (see Sects. 4.2, 4.3). Figure 3 shows the energy as a fraction of the total energy captured $\left(\rho_k/\rho_{total}\right)$ for each POD mode (k). For each corresponding mode, the typical wavelength $\lambda_{l,k}$ is determined along the meridian of the cone using $\lambda_{x,k}$ that is calculated by applying a 2D Fourier transform (F) on the image matrix of each POD mode. Note that the wavelength $\lambda_{l,k}$ is a dominant wavelength in the mode and is not necessarily the wavelength of the spiral vortices $\left(\lambda_l\right)$, since the flow field, in addition to the spiral vortices, also contains large-scale fluctuations relating to the vortex strength modulation. The Fast Fourier Transform (F) is computed in the region where the alternating fringes appear (in this case, it is $x/D = 0.6$ to 1.8, $y/D = -0.5$ to 0.5). The plot of normalized power spectral density ($|F|^2/\sigma^2M^2$) against the spatial frequencies f_x and f_y (along x and y directions, respectively) shows peaks corresponding to the dominant wavelength in the mode (see Fig. 6). Here, σ is root mean square (RMS) of the signal and M is the number of samples. The spectral resolution in the present case is $\delta f_x = 0.82/D$ and $\delta f_y = 0.96/D$. Uncertainty in wavelength estimation due to the finite spectral resolution is shown by means of error bars in Fig. 3. In a POD mode, the wavelength of the alternating fringes varies slightly when moving from the nose to the base, in proportion to the local cone radius (as seen in Fig. 4a). In addition, it can be observed in Fig. 3 that the dominant wavelength in some modes is significantly different from the neighbouring ones (e.g., modes 32, 36), and in the case of modes 20 and 23, it is out of the plot limits (larger than $1D$). Upon inspection of the mode, it appears that there are multiple wavelengths present (see Fig. 5). Therefore, the wavelength shown in Fig. 3 by itself is not a reliable measure to determine whether the POD mode directly corresponds to the spiral vortex structure or whether it represents the modulation of the vortex strength or the interaction of vortices. Therefore, it can only be used to qualitatively relate the energy distribution to the spatial periodicity of the fluctuations. Overall, it is observed that the wavelength decreases when the mode number increases (where energy decreases).

In addition, Fig. 3 also shows the typical number of fringe pairs (bright and dark) (n, equivalent to vortices as shown in Fig. 2) observed in the corresponding mode along the circumferential direction. As discussed before in Sect. 3, n is representative of the azimuthal wavelength λ_θ. As shown in Fig. 4b, n is calculated by tracking maxima/minima of I' along the y axis at every axial location. The number of fringe pairs on the back side of the cone (which is not visible) is assumed to be equal to the visible side. The maximum value of n observed in the POD mode at any axial location is assigned as a characteristic of the respective mode. In other words, it represents the minimum λ_θ observed. This can be used to determine whether the mode contributes to a physical representation of the spiral vortex or not (see Sect. 4.3). As n has to be an integer and the back side of the cone is not visible, the measurement uncertainty is ± 1.

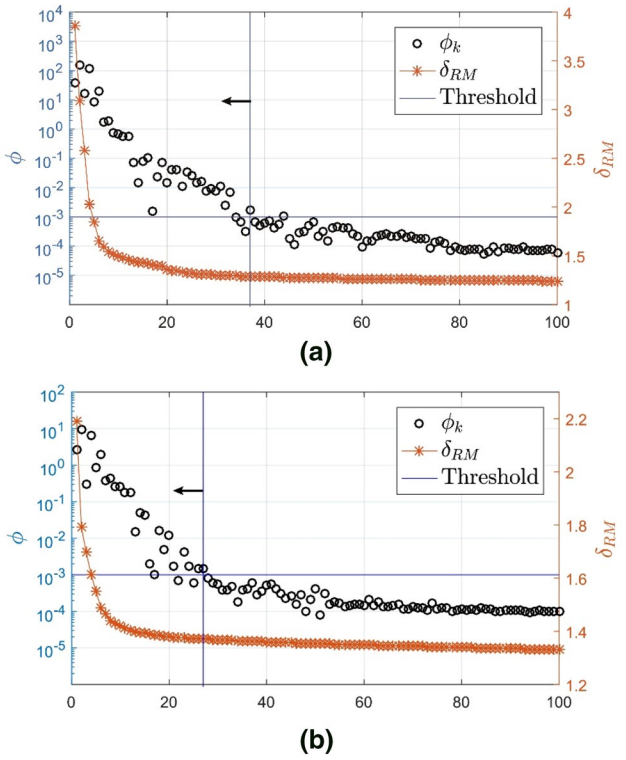

Fig. 7 Criterion used to define the threshold on the number of POD modes to be considered for a reconstruction **a** 5000 RPM, $k_{\text{thr}} = 37$, $\left(S_b = 5, Re_D = 7.4 \times 10^3, S = 0{-}4.71, Re_l = 0{-}1.58 \times 10^4\right)$, **b** 15,000 RPM, $k_{\text{thr}} = 27$, $\left(S_b = 5, Re_D = 2.3 \times 10^4, S = 0{-}4.71, Re_l = 0{-}4.7\times 10^4\right)$

4.2 Noise reduction

The first criterion is defined, such that certain POD modes which contain high noise levels are excluded without having a significant loss of flow information. In the literature (Raiola et al. 2015, 2017), a criterion to select the optimal number of POD modes for the reconstruction with reduced random noise has been proposed. This criterion is based on the consideration of the residual error $\delta_{\text{RM}}(k)$ involved in the reconstruction of the measured field using the first k number of modes. The threshold is set on the relative slope of $\delta^2_{\text{RM}}(k)$ and it has been shown that it significantly reduces the random noise in the low-order reconstruction. However, the reconstruction still includes the noise due to the focal plane arrays of the infrared camera (Raiola et al. 2017), as the POD modes corresponding to such noise usually have higher energy compared to the modes containing the random noise. However, in the present case, the objective of the reconstruction is to obtain the specific flow feature, i.e., the thermal footprints of the spiral vortices. Therefore, a different criterion is defined here that is based on the strength of these spiral vortices in a POD mode relative to the measurement noise.

A 2D Fourier transform (as discussed in Sect. 4.1) of each mode is used to identify the contribution of noise relative to the wavelengths of interest. Figure 6 shows the PSD distribution for the 15th and the 39th POD mode. It is evident that the 39th mode has overall low energy in the peaks as compared to the 15th mode; furthermore, a larger fraction of its energy is distributed among higher frequencies. In the present case, the wavelengths associated with the measurement noise are estimated to be of the order of 4 pixels ($\sim 0.024D$) and below. This is a choice dependent on the experimental conditions, flow structures of interest, and acceptable noise levels in the reconstruction. In the present case, temperature footprints of flow structures smaller than $0.024D$ are not expected to have a sufficient contrast with respect to the measurement noise. Therefore, the energy contained in wavelengths smaller than 4 pixels is regarded as noise $\left(E_{\text{noise}}\right)$. The energy distributed in the wavelengths of interest ($0.5D > \lambda_x, \lambda_y > 4$ pixels) is considered as the contribution to the signal $\left(E_{\text{signal}}\right)$. The typical energy corresponding to wavelengths λ_l larger than a certain wavelength λ_c can be obtained as follows:

$$E_{\lambda>\lambda_c} = \sum_{j=c}^{d} \sum_{i=a}^{b} \left|F_{i,j}\right|^2 \delta f_x \delta f_y, \tag{1}$$

where b and a are indices of f_xD corresponding to $\pm\left(1/\lambda_c - \delta f_x\right)D$, respectively. Similarly, d and c are indices of f_yD corresponding to $\pm\left(1/\lambda_c - \delta f_y\right)D$, respectively. $\lambda_c = 4\text{px} = 0.024D$ for $E_{\lambda>4\text{px}}$ and $\lambda_c = 0.5D$ for $E_{\lambda>0.5D}$. The energy associated with noise can be computed as follows:

$$E_{\text{noise}} = E_{\text{Total}} - E_{\lambda>4\text{px}}, \tag{2}$$

while the energy present in the signal can be obtained as follows:

$$E_{\text{signal}} = E_{\lambda>4\text{px}} - E_{\lambda>0.5D}. \tag{3}$$

Finally, the signal-to-noise ratio $E_{\text{signal}}/E_{\text{noise}}$ can be considered to represent the relative strength of a signal in a mode compared to noise. In addition, to account for the relative importance of each mode in the data set, the signal-to-noise ratio is multiplied with the fraction of energy captured in a POD mode with respect to the total energy $\left(\rho_k/\rho_{\text{total}}\right)$. In this way, a normalized signal strength ϕ_k may be defined as follows:

$$\phi_k = \frac{E_{\text{signal}}}{E_{\text{noise}}} \cdot \frac{\rho_k}{\rho_{\text{total}}}. \tag{4}$$

The order of threshold on ϕ_k in the present case is obtained by defining a threshold on $\rho_k/\rho_{\text{Total}} = 1 \times 10^{-4}$ and $E_{\text{signal}}/E_{\text{noise}} = 10$ which results in $\phi_k = 0.001$. This ensures that the POD modes with $\phi_k < 0.001$ have either low signal strength relative to noise or have overall low

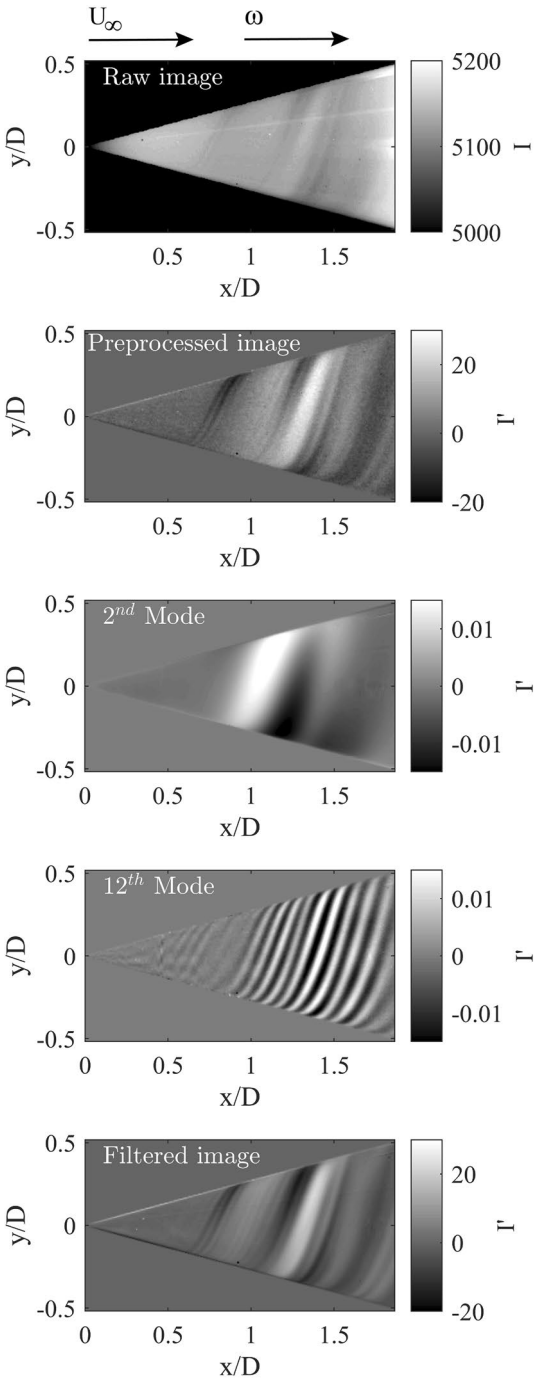

Fig. 8 POD-based reconstruction of spiral vortices from the instantaneous IR thermography data. Flow from left to right. $\phi_k > 0.001$, $k_{\text{thr}} = 37, (S_b = 5, Re_D = 7.4 \times 10^3, S = 0\text{–}4.71, Re_l = 0\text{–}1.58 \times 10^4)$

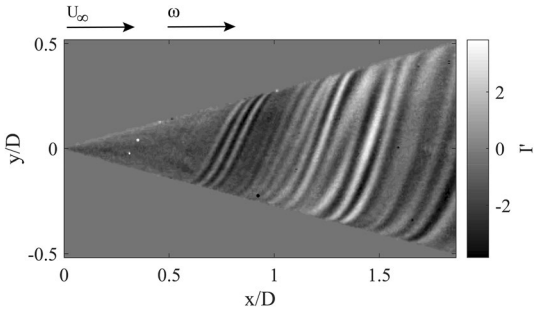

Fig. 9 Reconstruction using the POD modes satisfying the criteria: $\phi_k > 0.001$, $n \geq 8$. Flow is from left to right, $k_{\text{thr}} = 37$, $(S_b = 5, Re_D = 7.4 \times 10^3, S = 0\text{–}4.71, Re_l = 0\text{–}1.58 \times 10^4)$

energy content. It signifies that their effective contribution to the reconstruction of the signal is low, and therefore, their exclusion does not affect the objective of the reconstruction. The composition of ϕ_k is shown in Fig. 6 for modes above and below the defined threshold $\phi_k = 0.001$. It can be observed that the 15th mode in Fig. 6a has a high amount of energy distributed in the signal compared to the noise $\left(E_{\text{signal}}/E_{\text{noise}} = 66.27\right)$ and its overall importance in the data set is $\rho_k/\rho_{\text{Total}} = 1.24 \times 10^{-3}$. Together, the relative contribution of the mode in reconstructing the signal is $\phi_k = 0.082$. On the other hand, the 39th mode in Fig. 6b has a lower fraction of energy distributed in the signal compared to the noise $\left(E_{\text{signal}}/E_{\text{noise}} = 3.5\right)$ and its relative importance in the data set is significantly low $\rho_k/\rho_{\text{Total}} = 1.49 \times 10^{-4}$. Therefore, the relative contribution in reconstructing the signal becomes $\phi_k = 5.2 \times 10^{-4}$ which is lower by two orders of magnitude compared to that of the 15th mode.

The distribution of ϕ_k among the modes depends on the choice of the wavelengths that can be considered as a signal, which depend on the specific flow case and experimental conditions. Figure 7 shows the normalized signal strength $\left(\phi_k\right)$ and the residual error of reconstruction (δ_{RM}, represented in terms of I') corresponding to each mode for two different experimental conditions. In the present case, the last POD mode satisfying the criteria $\phi_k > 0.001$ is defined as the threshold k_{thr} and the reconstruction is done using the POD modes from 1 to k_{thr}.

Figure 8 shows the filtered image (reconstruction) obtained from the raw image. It can be observed that the camera noise has been effectively removed. However, the effect of large-scale modulations of local vortex strength is still present in the filtered image.

4.3 Physical admissibility of POD modes

The second criterion is defined to select modes that are physically admissible, i.e., those modes that can be directly linked to the structure of the vortices. This is done based on the physical characteristics of the spiral vortices. As discussed at the start of Sect. 4, the POD modes (excluding those containing measurement noise) can be further classified into roughly two contributions. First is the imprint due to the presence of the coherent vortices, and, second, the effects caused by the local modulation of the vortex

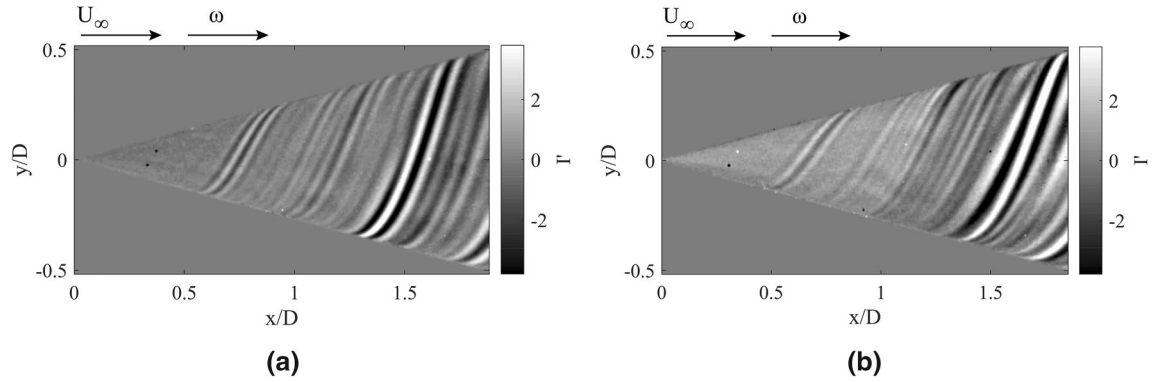

Fig. 10 Reconstruction using the POD modes satisfying the criteria: $\phi_k > 0.001$, $n \geq 8$. Flow is from left to right (**a**) $k_{\text{thr}} = 39$, $S_b = 4, Re_D = 9.6 \times 10^3, S = 0{-}3.77, Re_l = 1.97 \times 10^4$, (**b**) $k_{\text{thr}} = 44$, $S_b = 3, Re_D = 1.28 \times 10^4, S = 0{-}2.83, Re_l = 0{-}2.63 \times 10^4$

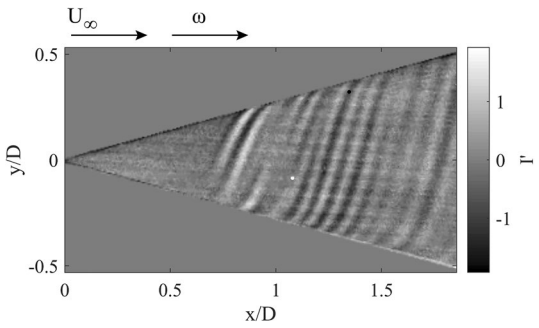

Fig. 11 Reconstruction using the POD modes satisfying criteria: $\phi_k > 0.001$, $n \geq 8$ for 15,000 RPM. Flow is from left to right $k_{\text{thr}} = 27$. $\left(S_b = 5, Re_D = 2.3 \times 10^4, S = 0{-}4.71, Re_l = 0{-}4.7 \times 10^4\right)$

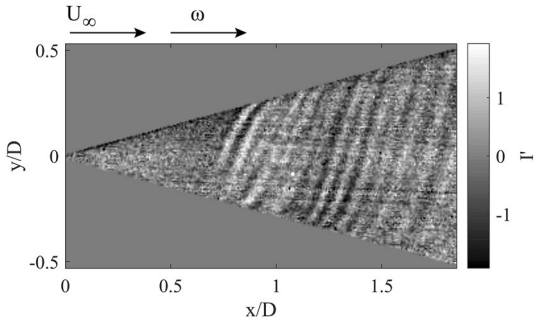

Fig. 12 Reconstruction using the criterion for noise reduction from the literature and: $n \geq 8$ for 15,000 RPM. Flow is from left to right. $k_{\text{thr}} = 193$. $\left(S_b = 5, Re_D = 2.3 \times 10^4, S = 0{-}4.71, Re_l = 0{-}4.7 \times 10^4\right)$

strength. In the present test case, previous experiments and theoretical analysis from literature show that the number of vortices (n) appearing in the boundary layer transition region varies with the local rotational ratio (S). From the study by Kobayashi et al. (1983), it is found that the number of vortices around the circumference at an axial location is always greater than or equal to 8. Similar results have also been reported in the theoretical study by Garrett et al. (2010), where they performed linear stability analyses on the range of broad cones (half angles $40° < \psi < 90°$). They observe that n decreases with increasing S but stays $n \geq 8$ even at $S \to \infty$. In these cases, spiral vortices occur due to cross-flow instability, which is different from the centrifugal instability observed in the present case, but still agrees with the lower bound on n. Similarly, the observed and predicted values of n for rotating spheres and disks are also greater than 8 (Kobayashi 1994). Physically, $n \geq 8$ implies that the $\lambda_\theta / r \leq \pi/4$ or $\theta \leq 45°$, where θ is the angle subtended by the azimuthal wavelength, see Fig. 2. In other words, these observations show that the perturbations with the azimuthal wavelengths longer than $\pi r/4$ (and $\theta > 45^o$) cannot grow to form the coherent spiral vortices. Also having, $n < 8$ implies $\lambda_\theta > \pi/4r$, and thus depending on the vortex angles would imply much larger vortices with respect to the local radius (e.g., $n = 2$, implies that $\lambda_\theta = \pi r$, which, for the typical vortex angles, would imply unreasonable vortex size). However, a more in-depth theoretical study is required to generalise this to any arbitrarily shaped body of revolution.

It can be said for the cases of rotating cones ($15° < \psi < 90°$), rotating sphere, and rotating disk (which is a rotating cone with $\psi = 90°$) that the POD modes corresponding to $n < 8$ do not physically resemble the spiral vortices, but are the effects of the large-scale modulations in local vortex strength. To separate the effect of the vortical structures from other large-scale phenomena, only modes with $n \geq 8$ are considered for the reconstruction. The selectively reconstructed image is shown in Fig. 9 revealing the spatial organization of the spiral vortices in detail. We

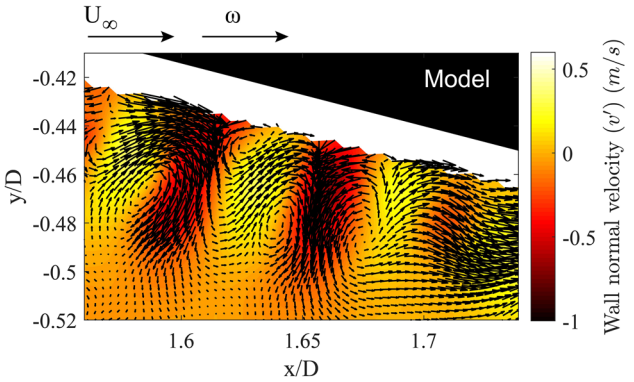

Fig. 13 Instantaneous vector field and contours of wall-normal velocity from stereo PIV with mean subtracted showing vortices produced over the cone surface. Flow from left to right $\left(S_b = 5, Re_D = 7.4 \times 10^3, S = 4.1{-}4.47, Re_l = 1.26 \times 10^4{-}1.45 \times 10^4\right)$

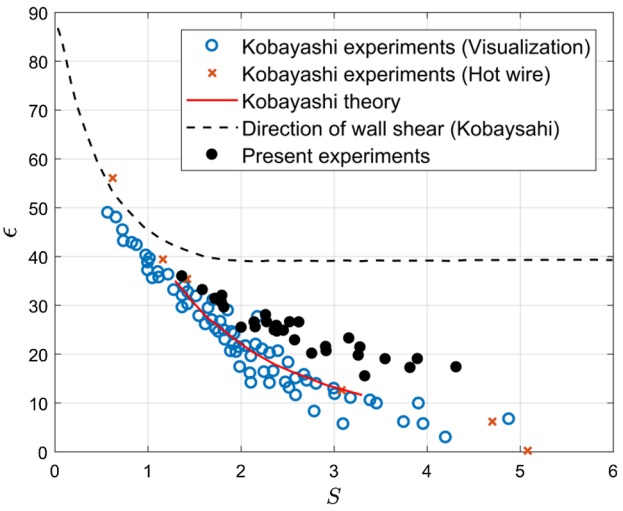

Fig. 15 Spiral vortex angle (ε) observed at each rotation ratio (S) compared with the results from the study by Kobayashi et al. (1983)

start observing spiral vortices from around $x/D = 0.6$. Their structure remains coherent and they grow in size as they move downstream until approximately $x/D = 1.2$ where the coherence in the spatial organization starts to decrease. This shows the onset of secondary instability on the vortices as the spacing between the two vortex lines appears to be varying azimuthally.

In addition, selectively reconstructed instances (based on criterion $n \geq 8$) for different combinations of S_b and Re_D are shown in Fig. 10. It can be observed that the spiral vortex angle (ε) and the number of spiral vortices (n) change as the distribution of the rotational ratio S changes over the cone surface. Figure 11 shows the similar result for $S_b = 5$ at 15,000 RPM. It is observed that the surface rotation during the integration time does not cause blur and spiral vortices are still observed. The difference between the vortex structure in Figs. 9 and 11 is due to the different Re_l.

As discussed at the start of Sect. 4.2, the application of the criterion proposed in the literature (Raiola et al. 2015, 2017) is not suitable in the present case, as the objective here is to reconstruct the thermal footprints of the spiral vortices. As an example, when this criterion is applied for the case shown in Fig. 11, the threshold mode number increases to $k_{\text{thr}} = 193$. It is clear in the corresponding distribution of ϕ_k from Fig. 7b that at mode numbers higher than 27, the signal strength drops considerably and there is no significant contribution to the signal relative to noise. Figure 12 shows the reconstruction where the criterion from the literature is used for the noise reduction. It is evident from the comparison between Figs. 11 and 12, that the higher noise is incorporated in the latter and there is no significant change in the structure of the spiral vortices.

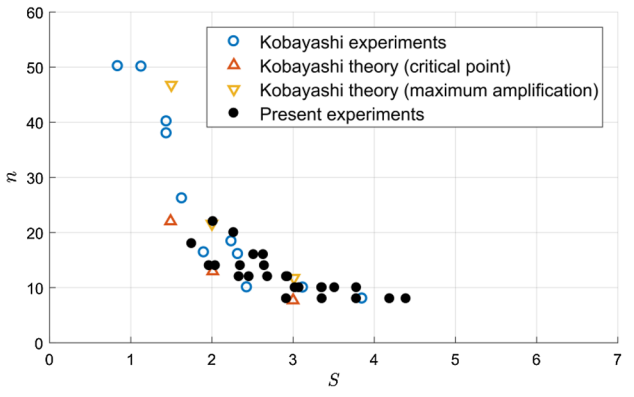

Fig. 14 Number of vortices (n) observed at each rotation ratio (S) compared with the experimental and theoretical results by Kobayashi et al. (1983)

When extending the present method to an arbitrarily shaped body of revolution, values of n can still be estimated as follows. The typical range of spiral vortex angles (ε) can be measured from the filtered image (as shown in Fig. 8). The stream-wise wavelength can be measured by means of other methods like PIV in the symmetry plane. Depending upon the geometry, λ_θ can be obtained from λ_x and ε, and, thus, a lower bound on $n = 2\pi r/\lambda_\theta$.

5 Comparison to PIV and literature

Figure 13 shows an instantaneous vector field from stereo PIV with the statistical average subtracted. The vector plot shows a cross-flow section of the spiral vortices near the wall. Measurement closer to the wall is not possible due to the laser reflection. It is clear from the vector fields that these vortices appear as pairs of counter-rotating vortices

with alternating mutual up-wash and down-wash regions. Comparing this with Figs. 8 and 9 shows that, indeed, the alternating dark and bright fringes observed in IRT correspond to the alternating mutual up-wash and down-wash regions of the vortices. Thus, between two bright (or dark) fringes in IRT images, there is one pair of counter-rotating vortices. The wavelength obtained from Fig. 13 is approximately $0.06D$, which is in the same order as the wavelengths in Fig. 3 corresponding to the POD modes with $n \geq 8$.

The number of spiral vortices (n) and spiral vortex angle (ε) are measured from the selective reconstructions for the different combinations of S_b and Re_D. They are plotted against the rotational ratio S and compared with the experimental and theoretical results from the study by Kobayashi et al. (1983) (see Figs. 14, 15). The comparison of n shows good agreement between the present study and the literature (see Fig. 14). The trend of spiral vortex angle (ε) is in agreement with the literature for small values of S, but it deviates from literature to higher angles at higher values of S (see Fig. 15). Note that measurements by Kobayashi et al. (1983) are performed away from the wall, while the angles in the present study are obtained from the measurements at the wall. Consequently, the angles in the present study deviate towards the direction of the local shear as seen in Fig. 15.

It shall be noted that the spiral vortices are superimposed on the flow and are convected over the cone surface. It is also evident from Fig. 13 that the vortices are observed only after subtraction of the mean flow. Thus, the limitation imposed on the present method comes from the blur caused by the convective velocity of the vortices during the integration time. The convective velocity is usually lower than the edge velocity. In the present study, the blur is lower than $0.01D$ to $0.05D$ for inflow velocities 2.46−12.3 m/s respectively. Therefore, reliable measurements of vortex number are only obtained from the flow cases with inflow velocity lower than 7.4 m/s (blur lower than $0.03D$).

6 Conclusion

It is shown that IRT coupled together with POD analysis proves to be a useful tool to understand the spatial organization of the non-stationary spiral vortices on rotating bodies of revolution. The criterion based on the signal-to-noise ratio is used to define the first threshold on the number of POD modes to obtain the reconstruction with reduced measurement noise. The results show a significant reduction in noise, without altering the structure of spiral vortices. Furthermore, the POD modes below the first threshold can be selectively used to separate the effect of local modulations in the spiral vortex strength and reconstruct the vortex structure based on the physical characteristics. It is observed from past studies that the number of vortices (n) along the azimuth is always greater than or equal to 8 for the cases of a rotating cone ($15° < \psi < 90°$), rotating sphere, and rotating disk. POD modes with the number of fringe pairs along the circumference (n) less than 8 are, therefore, excluded during reconstruction. The resulting reconstruction shows the spiral vortex structure, filtering out the effect of modulations in local vortex strength. The number of spiral vortices (n) is measured and found to be in a good agreement with the literature. Whereas, the measured spiral vortex angles (ε) show good agreement with those from the literature at low S, but deviate towards the direction of the local shear for higher S. This is a consequence of the measurements at the surface wall. The counter-rotating nature of spiral vortices has been confirmed by PIV measurements. Future work in this direction will include the application of this method to study the effect of non-axial inflow on the boundary layer transition region at higher Reynolds number. The method will also be applied to rotating bodies with different geometries as a part of further propulsion system studies.

References

Arányi P, Janiga G, Zähringer K, Thévenin D (2013) Analysis of different POD methods for PIV-measurements in complex unsteady flows. Int J Heat Fluid Flow 43:204–211. https://doi.org/10.1016/j.ijheatfluidflow.2013.07.001

Astarita T, Cardone G, Carlomagno GM, Tecchio P (2002) Spiral vortices detection on a rotating disk. In: ICAS 2002 CONGRESS. pp 1–8

Berkooz G, Holmes P, Lumley JL (1993) The proper orthogonal decomposition in the analysis of turbulent flows. Annu Rev Fluid Mech 25:539–575. https://doi.org/10.1146/annurev.fl.25.010193.002543

Garrett SJ, Peake N (2007) The absolute instability of the boundary layer on a rotating cone. Eur J Mech B/Fluids 26:344–353. https://doi.org/10.1016/J.EUROMECHFLU.2006.08.002

Garrett SJ, Hussain Z, Stephen SO (2010) Boundary-layer transition on broad cones rotating in an imposed axial flow. AIAA J 48:1184–1194. https://doi.org/10.2514/1.J050021

Kobayashi R (1994) Review: laminar-to-turbulent transition of three-dimensional boundary layers on rotating bodies. J Fluids Eng 116:200–211. https://doi.org/10.1016/j.ymssp.2015.09.042

Kobayashi R, Kohama Y, Kurosawa M (1983) Boundary-layer transition on a rotating cone in axial flow. J Fluid Mech 127:353–364. https://doi.org/10.1017/S0022112083002761

Kohama Y (1984) Behaviour of spiral vortices on a rotating cone in axial flow. Acta Mech 51:105–117. https://doi.org/10.1007/BF01177066

Mueller TJ, Nelson RC, Kegelman JT, Morkovin MV (1981) Smoke visualization of boundary-layer transition on a spinning axisymmetric body. AIAA J 19:1607–1608. https://doi.org/10.2514/3.60099

Narayanan V (2007) Oscillatory thermal structures in a reattaching jet flow. J Vis 10:389–396. https://doi.org/10.1007/BF03181897

Raiola M, Discetti S, Ianiro A (2015) On PIV random error minimization with optimal POD-based low-order reconstruction. Exp Fluids. https://doi.org/10.1007/s00348-015-1940-8

Raiola M, Greco CS, Contino M, Discetti S, Ianiro A (2017) Towards enabling time-resolved measurements of turbulent convective heat transfer maps with IR thermography and a heated thin foil. Int J Heat Mass Transfer 108:199–209. https://doi.org/10.1016/j.ijheatmasstransfer.2016.12.002

Ranc N, Blanche A, Ryckelynck D, Chrysochoos A (2015) POD preprocessing of IR thermal data to assess heat source distributions. Exp Mech 55:725–739. https://doi.org/10.1007/s11340-014-9858-2

Affiliations

Sumit Tambe[1] · Ferry Schrijer[1] · Arvind Gangoli Rao[1] · Leo Veldhuis[1]

✉ Arvind Gangoli Rao
a.gangolirao@tudelft.nl

[1] Faculty of Aerospace Engineering, Delft University of Technology, Delft, The Netherlands